MAGNETICALLY ALIGNED VELOCITY ANISOTROPY IN THE TAURUS MOLECULAR CLOUD

MARK HEYER,[1] HAO GONG,[1,2] EVE OSTRIKER,[2] AND CHRISTOPHER BRUNT[1,3]

ABSTRACT

Velocity anisotropy induced by MHD turbulence is investigated using computational simulations and molecular line observations of the Taurus molecular cloud. A new analysis method is presented to evaluate the degree and angle of velocity anisotropy using spectroscopic imaging data of interstellar clouds. The efficacy of this method is demonstrated on model observations derived from three-dimensional velocity and density fields from the set of numerical MHD simulations that span a range of magnetic field strengths. The analysis is applied to ^{12}CO $J = 1-0$ imaging of a subfield within the Taurus molecular cloud. Velocity anisotropy is identified that is aligned within $\sim 10°$ of the mean local magnetic field direction derived from optical polarization measurements. Estimated values of the field strength based on velocity anisotropy are consistent with results from other methods. When combined with new column density measurements for Taurus, our magnetic field strength estimate indicates that the envelope of the cloud is magnetically subcritical. These observations favor strong MHD turbulence within the low-density, subcritical, molecular gas substrate of the Taurus cloud.

Subject headings: ISM: clouds — ISM: individual (Taurus Molecular Cloud) — ISM: kinematics and dynamics — ISM: magnetic fields — methods: data analysis — MHD

Online material: color figures

1. INTRODUCTION

Dense, interstellar molecular clouds offer a unique and valuable laboratory to investigate magnetoturbulent phenomena. These clouds are expected to be fully turbulent systems with a very large dynamic range between driving and dissipation scales. The degree of magnetic coupling to the turbulent flows has important implications for the nature of gas dynamics and star formation within molecular clouds. A strong, well-coupled field can affect the star formation efficiency in a cloud by reducing the amount of material that is susceptible to gravitational collapse and star formation, and also affect the scale at which collapse occurs (Mouschovias 1976; Vazquez-Semadeni et al. 2005). Magnetic fields also strongly affect the degree of gas density compression in shocks. Such shock-generated density perturbations may provide the seeds of protostellar cores and protoclusters. Given the potential impact of the magnetic field on the gas dynamics of molecular clouds, it is imperative to measure (or estimate) magnetic field strengths and to develop accurate descriptions of magnetohydrodynamic (MHD) turbulence under conditions applicable in star-forming clouds.

Goldreich & Sridhar (1995, hereafter GS95) developed a theory for strong, incompressible, MHD turbulence that provides definitive predictions of the spectrum and anisotropy of velocity fields. Wave-wave interactions are expected to shear the Alfvén wave packet in the plane perpendicular to the mean field. Correspondingly, wave energy is more efficiently redistributed to smaller scales in the direction perpendicular to the field than through the cascade parallel to the field. GS95 propose that a critical balance is achieved between nonlinear interactions and wave propagation, such that the timescales to transfer energy along the two directions are comparable,

$$\lambda_{\parallel}/v_A \sim \lambda_{\perp}/v, \qquad (1)$$

[1] Department of Astronomy, University of Massachusetts, Amherst, MA 01003-9305; heyer@astro.umass.edu.
[2] Department of Astronomy, University of Maryland, College Park, MD 20742-2421; hgong@astro.umd.edu, ostriker@astro.umd.edu.
[3] School of Physics, University of Exeter, Stocker Road, EX4 4QL, UK; brunt@astro.ex.ac.uk.

where $\lambda_{\parallel}$ and $\lambda_{\perp}$ are the wavelengths parallel and perpendicular to the mean field and v is the mean velocity fluctuation at the scale of the corresponding component. For an energy-conserving cascade, $v \propto \lambda_{\perp}^{1/3}$, so equation (1) implies

$$\lambda_{\parallel} \propto \lambda_{\perp}^{2/3}. \qquad (2)$$

The corresponding velocity scaling law along the magnetic field is $v \propto \lambda_{\parallel}^{1/2}$. A critically balanced Alfvénic cascade leads to a scale-dependent anisotropy of the velocity field. This anisotropy has been demonstrated with computational simulations for both incompressible and compressible MHD turbulence (e.g., Maron & Goldreich 2001; Cho et al. 2002; Vestuto et al. 2003).

Can MHD-induced velocity anisotropy, as predicted by GS95, be measured in interstellar clouds? Watson et al. (2004) and Wiebe & Watson (2007) have attributed the polarization properties of both OH masers and thermal molecular line emission to directionally dependent optical depths induced by MHD turbulence. More panoramic observational views of the gas dynamics rely on spectroscopic imaging data of atomic or molecular line emission, most notably, the H I 21 cm line, and the low-rotational transitions of ^{12}CO and its isotopomers, ^{13}CO and C^{18}O. In principle, the spatial variation of line shapes and velocity displacements offers a proxy view of the prevailing cloud dynamics. Recovering the form of the velocity power spectrum or its equivalent structure function from the spectroscopic data cubes, $T(x, y, v)$, is challenging, owing to the complex integration of the velocity and density fields along the line of sight and the effects of line excitation and opacity that may filter or mask dynamical information from some fraction of the volume (Brunt & Mac Low 2004; Ossenkopf et al. 2006).

Principal component analysis (PCA) is a powerful method to examine spectroscopic imaging data of interstellar clouds. It reorders the data onto a set of eigenfunctions and eigenimages (Heyer & Schloerb 1997; Brunt & Heyer 2002). Characteristic velocity differences, δv, and spatial scales, τ, are derived for each principal component for which the signal variance is distinguished from the statistical noise of the data. The set of δv, τ points can be

empirically linked to the true velocity structure function using model velocity and density fields (Brunt & Heyer 2002; Brunt et al. 2003). The method has been applied to a large set of ^{12}CO and ^{13}CO imaging observations of giant molecular clouds located within 4 kpc of the Sun to establish the universality of turbulence within the molecular interstellar medium (Brunt 2003; Heyer & Brunt 2004). However, these studies did not consider velocity anisotropy. The eigenvectors were derived from the covariance matrix that was accumulated from all spectra within the data cube with no orientation constraints. Therefore, any dynamical signature of anisotropy along a given axis was necessarily diluted by isotropic contributions to the covariance matrix. The corresponding eigenimages identified locations within the projected plane where velocity differences can occur but at any angle.

In this paper we describe a modified application of PCA on spectroscopic imaging data to recover structure functions along perpendicular axes (§ 2). In § 3 the utility of this analysis is demonstrated on spectroscopic data cubes derived from model velocity and density fields from decaying MHD simulations covering a range of magnetic field strengths. In § 4 we apply this analysis to ^{12}CO $J = 1–0$ observations of a subfield within the Taurus molecular cloud to show that such anisotropy is present and that the degree of anisotropy provides a coarse estimate to the strength of the magnetic field in this region.

2. DESCRIPTION OF ANALYSIS METHOD: AXIS-CONSTRAINED COVARIANCE MATRIX

To examine the degree of velocity anisotropy in interstellar clouds we have made a simple modification to the application of principal component analysis. A directional constraint is imposed on the eigenvectors by calculating the covariance matrix from the sequence of spectra along one spatial axis (position-velocity slices of the data cube). The position-velocity image can be extracted one slice at a time to preserve spatial resolution or can be generated by averaging contiguous slices to increase the signal-to-noise ratio. For a given data cube, $T(x, y, v)$, with dimensions n_x, n_y, n_v, the position-velocity slice along the x-direction, averaged over thickness Δ in the y-direction, is

$$W_y(x, v) = \frac{1}{\Delta} \sum_{j=j1}^{j2} T(x, y_j, v), \qquad (3)$$

where $\Delta = j2 - j1 + 1$. The covariance matrix for this position-velocity slice, $\mathbf{C}^x$, has components

$$C_{kl}^x = \frac{1}{n_x} \sum_{i=1}^{n_x} W(x_i, v_k) W(x_i, v_l), \qquad (4)$$

(suppressing the y subscript on W). The eigenvalue equation is solved for this axis-constrained covariance matrix,

$$\mathbf{C}^x u_x = \lambda_x u_x, \qquad (5)$$

to produce the set of n_v eigenvectors, $u_x(v)$, that describe velocity differences *exclusively* along this particular position-velocity slice. To spatially isolate where these differences occur for each component, the spectra are projected onto the corresponding eigenvector,

$$I_x(x_i) = \sum_{k=1}^{n_v} W(x_i, v_k) u_x(v_k). \qquad (6)$$

The eigenprojection, $I_x(x)$, has dimensions $n_x \times 1$. The characteristic velocity difference, δv_x, and scale, τ_x, are determined from the scale length of the normalized autocorrelation functions of $u_x(v)$ and $I_x(x)$, respectively (Brunt & Heyer 2002). Typically, only 4–5 $(\delta v, \tau)$ pairs can be extracted from the axis-constrained eigenvectors and projections for a given position-velocity slice, owing to the limited spatial dynamic range. These steps are repeated for all position-velocity slices ($j1 = 1, 1 + \Delta, 1 + 2\Delta$, ..., $n_y - \Delta$) in the data cube to produce a composite set of $(\delta v_x, \tau_x)$ pairs derived from n_y/Δ sets of eigenvectors and eigenprojections. Similarly, to examine structure along the y-axis, these steps are applied to position-velocity slices along the y-direction averaged over x-thickness $\Delta = i2 - i1 + 1$,

$$W_x(y, v) = \frac{1}{\Delta} \sum_{i=i1}^{i2} T(x_i, y, v), \qquad (7)$$

with covariance matrix

$$C_{kl}^y = \frac{1}{n_y} \sum_{j=1}^{n_y} W(y_j, v_k) W(y_j, v_l). \qquad (8)$$

A corresponding set of $(\delta v_y, \tau_y)$ pairs are derived from n_x/Δ sets of eigenvectors, $u_y(v)$, and eigenprojections, $I_y(y)$. For each axis, we consolidate the τ values into 1 pixel wide bins and calculate the mean and standard deviation of δv values for each bin. Power laws are fit to each set to derive a relationship between the magnitude of velocity differences in the line profiles and scale over which these differences occur, when constrained to each axis,

$$\langle \delta v_x \rangle = v_{0,x} \tau_x^{\alpha_x}, \qquad (9a)$$

$$\langle \delta v_y \rangle = v_{0,y} \tau_y^{\alpha_y}. \qquad (9b)$$

The PCA scaling exponents, α_x, α_y, are empirically linked to the scaling exponents of the first-order velocity structure function (Brunt et al. 2003).

$$\gamma = 1.69\alpha - 0.54, \qquad \alpha \le 0.67, \qquad (10a)$$

$$\gamma = 0.93\alpha - 0.03, \qquad \alpha > 0.67. \qquad (10b)$$

The first-order structure functions, $\delta v_x = v_{0,x} \tau_x^{\gamma_x}$ and $\delta v_y = v_{0,y} \tau_y^{\gamma_y}$, provide equivalent information to the power spectrum of the velocity field along the k_x- and k_y-axes, respectively, for $k_z = 0$. Averaging over Δ in y (or in x) is equivalent to integrating along k_y (or k_x).

This method offers a tool to derive velocity structure functions along any two perpendicular (spatial) axes of a spectroscopic data cube. With a priori knowledge of the local magnetic field direction, one could simply rotate the data cube to align the x-axis along this direction and determine the parallel and perpendicular structure functions. However, this orientation may not necessarily correspond to the angle at which velocity anisotropy is largest. A more rigorous test of MHD-induced anisotropy is the demonstration that velocity anisotropy is *maximized* when one of the two orthogonal axes lies along the local magnetic field direction. To determine the angle of maximum anisotropy, θ_{MAX}, the spectroscopic data cube is rotated through a sequence of angles, θ, in the plane of the sky from which the x- and y-axis structure functions are calculated for each angle. To compare with polarization

TABLE 1
MHD Simulation Parameters

Model	β	t/t_s	M_s
B2..............................	0.01	0.07	7.4
C2..............................	0.10	0.04	7.6
D2..............................	1.00	0.05	7.2
B3..............................	0.01	0.19	4.9
C3..............................	0.10	0.09	4.9
D3..............................	1.00	0.09	4.9

observations that measure position angles east of north, we define θ as the angle measured counterclockwise from the y-axis. To quantify the difference between the x- and y-axis structure functions for each angle, we consider two separate measures of anisotropy. The first anisotropy index, Ψ_1, is motivated by GS95, who predict differences in the scaling exponents, γ_x, γ_y,

$$\Psi_1 = \frac{\gamma_x - \gamma_y}{\gamma_x + \gamma_y}. \qquad (11)$$

Based on the results shown in §§ 3.1 and 3.3, the second anisotropy index, Ψ_2, measures the difference between the normalization constants, $v_{0,x}, v_{0,y}$,

$$\Psi_2 = \frac{v_{0,y} - v_{0,x}}{v_{0,y} + v_{0,x}}. \qquad (12)$$

For an isotropic velocity field, $\Psi_1 \approx 0$ and $\Psi_2 \approx 0$.

The modulation of Ψ by position angle enables a more accurate determination of the amplitude and angle at which the velocity anisotropy is maximized. This modulation involves rotation about an axis, so there is degeneracy for angles θ and $\theta + 180$. We find that the function

$$\Psi(\theta) = \Psi_0 \cos[2(\theta - \theta_{\mathrm{MAX}})] \qquad (13)$$

provides a reasonable fit to the variation of the anisotropy index. The coefficient Ψ_0 gives the amplitude of the anisotropy, and the phase θ_{MAX} is the angle of maximum anisotropy that can be compared to the local field direction $\langle \theta_B \rangle$.

3. MHD SIMULATIONS

To demonstrate that the analysis described in § 2 can indeed recover the spatial statistics of the velocity field, we have analyzed a set of computational simulations of decaying MHD turbulence from Ostriker et al. (2001). The models span a range of magnetic field strengths parameterized by the ratio of thermal to mean-field magnetic energy densities, $\beta = c_s^2/v_A^2$, where c_s is the sound speed for H_2 and v_A is the Alfvén velocity based on the mean field, $\langle B \rangle (4\pi\rho)^{-1/2}$. In these decaying-turbulence simulations, the initial velocity field is identical for all models, so any subsequent differences in the velocity field (including anisotropy) arise due to magnetic effects. For each β model ($\beta = 0.01, 0.1$, and 1), we examine two snapshots at times t in units of the sound crossing time, t_s. The snapshots are chosen such that the kinetic energy, or sonic Mach number $M_s = v_{\mathrm{rms}}/c_s$, is comparable for all β. A summary of the simulation snapshots is listed in Table 1. The cloud models are initially threaded with a spatially uniform magnetic field along axis 1 of the volume [$B_0 = (B_1, 0, 0)$]; owing to periodic boundary conditions adopted for the simulations, the mean field $\langle B \rangle = B_0$ at all times, although the total magnetic

field strength $|B|$ changes in time. Depending on the strength of the mean magnetic field, B_0, turbulent flows can distort the magnetic field lines.

A coarse estimate to the large-scale magnetic field alignment is provided by the variance of each component B_1, B_2, and B_3 normalized by the total field $B = (B_1^2 + B_2^2 + B_3^2)^{1/2}$. For the strong-field simulation ($\beta = 0.01$; snapshots B2, B3) the variance of the magnetic field components on each axis is small ($<3\%$), indicative of a spatially rigid field well aligned along axis 1 for most cells within the volume. For the intermediate- ($\beta = 0.1$; snapshots C2, C3) and weak-field ($\beta = 1$; snapshots D2, D3) cases the fluctuations of the field values are significantly larger (10%–40%), reflecting localized tangling of the magnetic field.

3.1. Direct Measurement of Velocity Anisotropy

The MHD velocity anisotropy is manifest by the spectral properties of the velocity field along axes parallel and perpendicular to the magnetic field. Cho et al. (2002) and Vestuto et al. (2003) examined the spectral slopes of directional power spectra or equivalently, the second-order structure function, of velocity fields from computational simulations. Both studies found steeper spectral slopes and smaller normalization constants for structure functions extracted along the magnetic field direction relative to those along an axis perpendicular to the field. That is, the velocity field contains more power when $k_\perp \approx k$ and $k_\parallel \approx 0$ than when $k_\parallel \approx k$ and $k_\perp \approx 0$, for a given k.

To quantify the velocity anisotropy in the simulations used in this study and to compare with simulated observations shown in § 3.2, the true second-order structure function, $S_2(\tau)$, is calculated directly from each model velocity field, v_2,

$$S_2(\tau_\parallel, \tau_\perp) = \left\langle [v_2(\boldsymbol{x}) - v_2(\boldsymbol{x} + \tau)]^2 \right\rangle, \qquad (14)$$

where $\tau = \tau_\parallel \boldsymbol{e}_\parallel + \tau_\perp \boldsymbol{e}_\perp$; $\boldsymbol{e}_\parallel$ and $\boldsymbol{e}_\perp$ are unit vectors parallel and perpendicular, respectively, to the local mean magnetic field direction, and the angle brackets denote a spatial average over the volume (Cho et al. 2002). Here we restrict our analysis to the projected plane appropriate for the velocity field to facilitate comparison with model observations in § 3.2. In this case the v_2 component projects into the plane[4] defined by axes 1 and 3. Figure 1 shows the second-order structure functions, $S_2(0, \tau_\perp)$ and $S_2(\tau_\parallel, 0)$. Power laws are fit over the pixel range 5–15 to exclude the steep component at small scales that results from grid-scale numerical dissipation of the simulation. The amplitudes and spectral indices of an equivalent, first-order structure function, $(S_2)^{1/2}$, are listed in Table 2. Velocity anisotropy is clearly identified in the B2 and B3 simulation snapshots, as the slope and amplitude of the orthogonal structure functions are different. For the intermediate (snapshots C2, C3) and weak (snapshots D2, D3) B field cases, the structure functions are statistically equivalent, indicative of globally isotropic velocity fields with slopes (~ 0.5) that are typical of strongly supersonic, super-Alfvénic turbulent flows. The absence of velocity anisotropy results from the local distortions of the magnetic field that dilute any signature to large-scale anisotropy.

3.2. Model Spectroscopic Data Cubes

Observers do not directly recover the three-dimensional velocity fields. Wide-field spectroscopic imaging measures line intensity

---

[4] To distinguish between the three spatial coordinate axes of the models and the observed projected axes we reference the three spatial axes of the model fields as 1, 2, 3 and label the projected, observed axes as x and y.
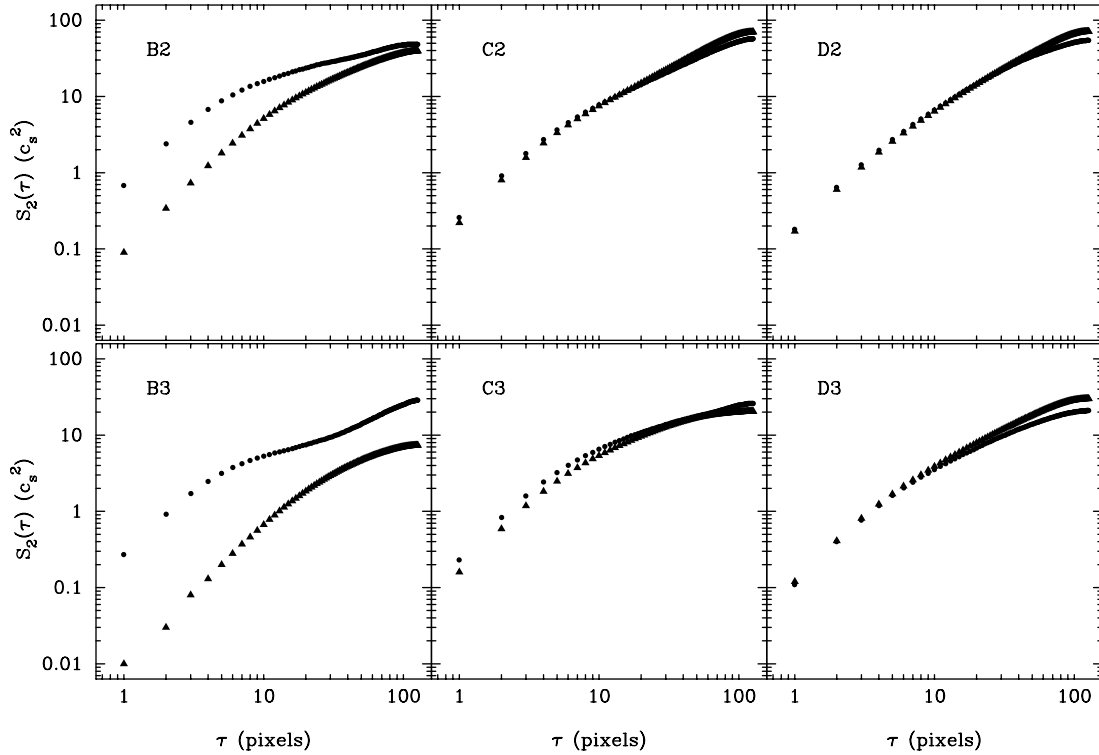
FIG. 1.—Second-order velocity structure function, $S_2(\tau)$, along axes parallel (*triangles*) and perpendicular (*circles*) to the mean magnetic field direction for velocity fields from turbulent simulations. Velocity anisotropy is evident in the strong-field model cases (B2, B3) as a larger scaling amplitude and shallower index for the structure function perpendicular to the mean field direction. [*See the electronic edition of the Journal for a color version of this figure.*]

as a function of position on the sky and velocity along an axis. The precise shape of a line profile is dependent on density, the projected velocity component, temperature, and chemical abundance that are integrated along the line of sight and affected by line excitation and opacity. To place the model velocity and density fields from the computational simulations in the same domain as observations we generate synthetic line profiles of ^{12}CO and ^{13}CO $J = 1-0$ emission. Details of the line excitation and radiative transfer calculations are described by Brunt & Heyer (2002). The assumed abundance values of ^{12}CO and ^{13}CO relative to H$_2$ are 1.0×10^{-4} and 1.25×10^{-6}, respectively. We adopt a uniform kinetic temperature of 15 K, which corresponds to a one-dimensional sound speed of 0.22 km s^{-1}. The adopted mean volume density of H$_2$ is $n = 1000$ cm^{-3}.

The choice of constructing synthetic profiles of the high-opacity ^{12}CO emission is motivated by two factors. First, the ^{12}CO $J = 1-0$ line is the most common tracer of cloud structure, so there are many observational data sets available to compare with these models. To be sure, ^{12}CO does not effectively probe the high-density cores of molecular clouds where star for-

mation takes place. However, these regions comprise a small fraction of the cloud mass and volume (Heyer et al. 1996; Goldsmith et al. 2008). Brunt & Heyer (2002) examined the effects of line opacity on the gas dynamics perceived by observations. With the exception of microturbulent velocity fields, they found that ^{12}CO measurements reliably recover the velocity field statistics. Although the local optical depth can be large within a volume, the macroturbulent velocity fields provide an effective large velocity gradient condition that allows most photons from the surface of the local volume to escape. In addition, owing to radiative trapping, ^{12}CO is detected over a broader area than the lower opacity lines, so there are simply more measurements and information on the largest scales. Nevertheless, to re-examine the effects of line opacity, we also generate and analyze synthetic profiles of the ^{13}CO $J = 1-0$ transition.

3.3. *Axis-Constrained PCA Applied to Model Data Cubes*

The utility of the analysis described in § 2 is assessed by its application to the synthetic ^{12}CO and ^{13}CO data cubes constructed from the MHD model density and velocity fields. Does the analysis recover velocity anisotropy when this is present in the raw velocity field, for the case of strong magnetic fields? Does the method verify isotropic velocity fields in the intermediate- and weak-field cases?

Here we examine the synthetic spectroscopic data cubes derived from the v_2 velocity field for position angle $\theta = 90°$, i.e., corresponding to alignment of the x-axis with the mean magnetic field direction in the plane of the sky. The results of the axis-constrained PCA method (with $\Delta = 2$), as applied to all model snapshots, are shown in Figure 2. Magnetically aligned anisotropy is clearly identified for the B2 and B3 simulation snapshots as a separation of the set of points $(\langle \delta v \rangle, \tau)$ derived, respectively,

TABLE 2
STRUCTURE FUNCTION PARAMETERS: $[S_2(\tau)]^{1/2} = v_0 \tau^\gamma$

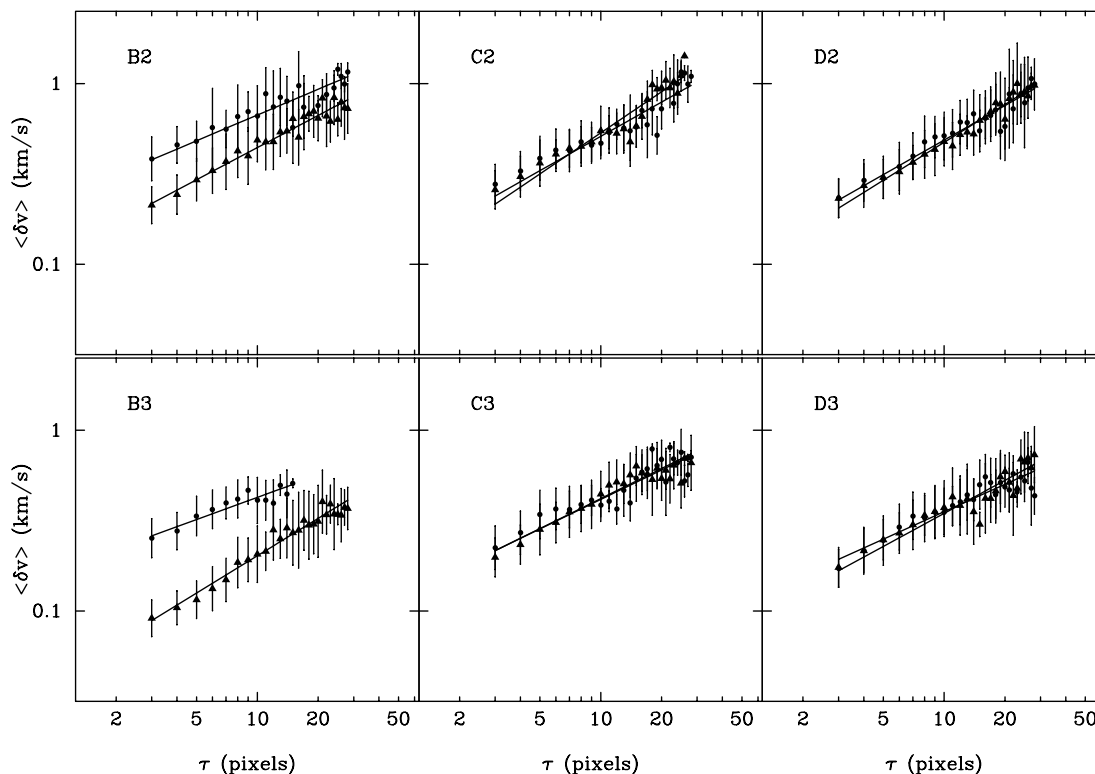| Model	$\gamma_\parallel$	$\gamma_\perp$	$v_{0,\parallel}$	$v_{0,\perp}$
B2	0.68	0.35	0.47	1.76
C2	0.53	0.49	0.80	0.89
D2	0.63	0.61	0.60	0.63
B3	0.82	0.29	0.14	1.16
C3	0.49	0.44	0.74	0.92
D3	0.56	0.52	0.54	0.57

Fig. 2.—Axis-constrained PCA $\langle\delta v\rangle, \tau$ relationships derived from synthetic spectroscopic data cubes of ^{12}CO $J = 1-0$ emission for the x-axis (along the mean magnetic field; *triangles*) and y-axis (perpendicular to the mean magnetic field; *circles*). The error bars reflect the standard deviation of values within each 1 pixel wide bin of τ. The method recovers the anisotropy intrinsic to the B2 and B3 model velocity fields and verifies the isotropic velocity fields of the intermediate- (C2, C3) and weak-field (D2, D3) models. [*See the electronic edition of the Journal for a color version of this figure.*]

along the x- and y-axes of the model data cubes. This separation of points is qualitatively similar to the corresponding true structure functions calculated directly from the velocity fields that are shown in Figure 1. For the intermediate (C2, C3) and weak (D2, D3) magnetic field snapshots, there is a strong overlap of points $(\langle\delta v\rangle, \tau)$ derived for the orthogonal axes. This indicates velocity isotropy with respect to the mean magnetic field and is in agreement with the true velocity structure functions for the models.

To assess the method quantitatively, bisector fits of power laws with parameters α and v_0, are fit to each set of points for each axis over the range 3 pixels $\leq \tau \leq 30$ pixels. The scaling exponents, $\gamma_\parallel$ and $\gamma_\perp$, of the structure function are derived from the fitted parameters, $\alpha_\parallel$ and $\alpha_\perp$, according to equation (10). The results for the ^{12}CO and ^{13}CO model data cubes are summarized in Table 3. With the exception of the C3 model data cube, there are no significant differences between the power-law parameters derived from ^{12}CO and ^{13}CO model cubes, demonstrating that opac-

ity effects do not significantly skew the derived velocity field statistics.

For the strong-field simulations, the separation of points in Figure 2 is due to a combination of a larger normalization constant and shallower index for the perpendicular structure function. Moreover, the anisotropy is stronger in the later stage simulation (comparing B3 with B2). There are, however, discrepancies between the values of γ determined directly from the velocity field in Table 2 and those determined by PCA that are listed in Table 3. The rms difference between power-law indices is 0.12 (23%). This discrepancy is due in part to the difficulty in measuring a power-law index of structure functions of velocity fields produced by the computational simulations that have limited inertial range (Vestuto et al. 2003). In addition, the PCA eigenprojection along a single axis tends to limit the dynamic range of spatial scales over which the power-law parameters are derived. Despite this discrepancy of the scaling exponents, these results demonstrate the ability of

TABLE 3
STRUCTURE FUNCTION PARAMETERS DERIVED FROM MODEL DATA CUBES

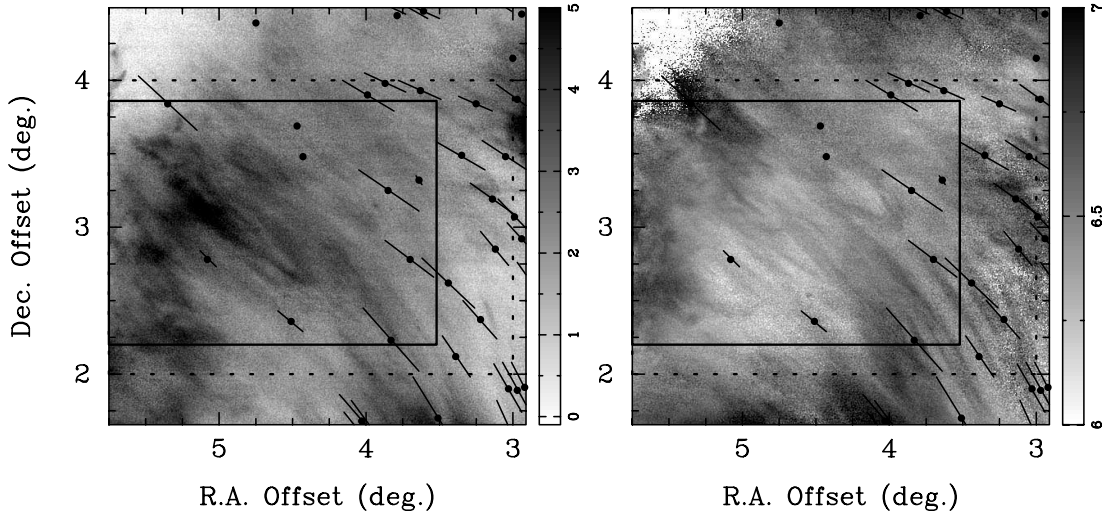| MODEL	^{12}CO				^{13}CO			
	$\gamma_\parallel$	$\gamma_\perp$	$v_{0,\parallel}$	$v_{0,\perp}$	$\gamma_\parallel$	$\gamma_\perp$	$v_{0,\parallel}$	$v_{0,\perp}$
B2	0.46	0.26	0.11	0.23	0.55	0.32	0.08	0.15
C2	0.67	0.53	0.09	0.12	0.57	0.44	0.10	0.12
D2	0.62	0.53	0.10	0.11	0.53	0.59	0.10	0.10
B3	0.61	0.15	0.04	0.17	0.62	0.23	0.04	0.13
C3	0.38	0.39	0.12	0.12	0.34	0.53	0.10	0.08
D3	0.49	0.31	0.09	0.11	0.61	0.41	0.07	0.09

Fig. 3.—(*Left*) Image of ^{12}CO $J = 1-0$ emission of a subfield within the Taurus molecular cloud integrated over the velocity interval 5.5–7.5 km s^{-1} and (*right*) image of ^{12}CO velocity centroid (Narayanan et al. 2008), with overlay of optical polarization vectors from the compilation by Heiles (2000). The molecular line emission and velocities exhibit streaks that are aligned along the local magnetic field direction. The solid line box outlines the area on which the axis-constrained PCA method is applied. The dotted-line box shows the area within which the polarization angles are averaged to estimate the mean magnetic field direction.

the axis-constrained PCA eigenfunctions to show a clear signature of velocity anisotropy induced by MHD turbulence.

4. THE TAURUS MOLECULAR CLOUD

The Taurus molecular cloud provides a valuable platform to investigate interstellar gas dynamics and the star formation process, owing to its proximity (140 pc) and the wealth of complementary data. Narayanan et al. (2008) present new wide-field imaging observations of ^{12}CO and ^{13}CO $J = 1-0$ emission from the central 100 deg^2 of the Taurus cloud complex, obtained with the FCRAO 14 m telescope. The images identify a low column density substrate of gas that contains subtle streaks of elevated ^{12}CO emission aligned along the local magnetic field direction as determined from stellar polarization measurements (Heiles 2000). Images of ^{12}CO $J = 1-0$ integrated intensity and centroid velocity with measured polarization vectors from this subfield are shown in Figure 3. These show a connection between the density and velocity fields. While the origin of these streaks is unknown, their rigorous alignment with the polarization vectors strongly suggests that the interstellar magnetic field plays a prominent role in the gas dynamics of this low-density material.

To assess the degree of velocity anisotropy within this subregion of the Taurus molecular cloud, we have applied the axis-constrained PCA method to the ^{12}CO data from this imaging survey. The precise field is described by the solid box in Figure 3. We do not consider the ^{13}CO $J = 1-0$ data, since the signal is weak from this low column density sector of the cloud. The mean, local polarization angle, derived from 16 measurements within the field, is $52° \pm 10°$. Assuming that the polarization is induced by selective absorption of background starlight by magnetically aligned, elongated dust grains, this angle corresponds to the local magnetic field direction (Purcell 1979; Draine 2003). Figure 4 shows the variation of the anisotropy indices, Ψ_1 and Ψ_2, with position angle (measured east of north) for ^{12}CO data within this subfield of the Taurus cloud. For Ψ_1, which considers the differences in scaling exponents, the fitted parameters are $\Psi_0 = 0.49 \pm 0.03$ and $\theta_{MAX} = 41° \pm 2°$. For Ψ_2, which measures anisotropy based on the differences of the normalization constants, $\Psi_0 = 0.56 \pm 0.03$ and $\theta_{MAX} = 46° \pm 2°$. The angle of maximum anisotropy is within $6°$–$11°$ of the local magnetic field direction

and the mean position angle of the emission streaks of ^{12}CO emission. The x- and y-axis structure functions derived at $\theta_{MAX} = 46°$ are shown in Figure 5. These distributions show the same pattern of offsets between the parallel and perpendicular structure functions measured in the strong-field simulation snapshots (B2, B3) shown in Figure 2. For the Taurus field, the power-law index of the structure function derived from ^{12}CO along the x-axis (i.e., the direction aligned with the polarization) is steeper (0.81 ± 0.05) than the index of the y-axis structure function (0.34 ± 0.06). The steeper power law along the x-axis is indicative of a velocity field more dominated by large scales. Similar to the model structure functions in the strong magnetic field cases, the normalization of the y-axis structure function, $v_{0,y}$, is 0.08 km s^{-1} and larger than the value of the x-axis structure function ($v_{0,x} = 0.02$ km s^{-1}). Thus, the smooth variation of density along the presumed magnetic field is mirrored by a smooth variation in the velocity, and the stronger variation in density in the perpendicular direction (streakiness) is mirrored by a stronger variation in the velocity. Indeed, preliminary analysis shows that in the direction perpendicular to the projected magnetic field, displacements between the peaks in integrated intensity and velocity centroids are similar with typical values 0.2–0.4 pc.

The results shown in Figures 3, 4, and 5 are suggestive of velocity anisotropy induced by strong MHD turbulence, as described by GS95 and verified by computational simulations (Cho et al. 2002; Vestuto et al. 2003). We note that the observed spectral slope parallel to the field, $\gamma_\parallel$, is steeper than the value predicted for incompressible MHD turbulence by GS95 but is similar to values derived for the strong-field (B2, B3) simulations. Velocity anisotropy could be produced by processes other than MHD turbulence. A systematic flow of material that is "channeled" by the magnetic field may also generate differences in the parallel and perpendicular structure functions. Such large-scale gradients would produce steep spectral indices ($\gamma \geq 1$). However, the observed high-frequency variation of velocities perpendicular to the field is not characteristic of such large-scale shear flows. Regardless of its origin, the near alignment of the velocity anisotropy with the local magnetic field direction demonstrates the importance of the interstellar magnetic field to the gas dynamics within this low-density component of the Taurus molecular cloud.
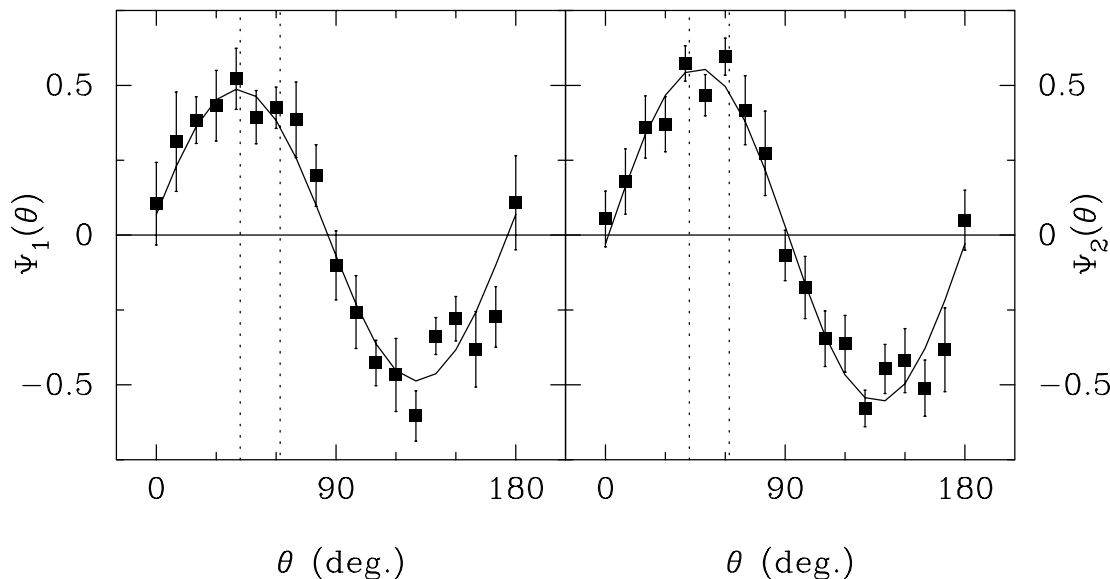
FIG. 4.—Variation of the anisotropy indices, Ψ_1 (*left*) and Ψ_2 (*right*), with position angle, θ. For each index, the solid line shows the fit of eq. (13) to the set of points. The dashed vertical lines show $\langle\theta_B\rangle \pm 1\,\sigma$ inferred from optical polarization measurements of background stars within the subfield. The angle of maximum anisotropy is nearly aligned with the local magnetic field direction, which suggests a relationship between velocity anisotropy and the interstellar magnetic field induced by strong MHD turbulence.

4.1. *The Magnetic Field Strength in the Taurus Cloud Envelope*

Since anisotropy is only evident in models with strong magnetic fields, the identification of such anisotropy within observational data offers a proxy measure of the magnetic field and its effect on the neutral gas (Vesuto et al. 2003). Specifically, the amplitude of the mean magnetic field, $B_0 = |\langle\boldsymbol{B}\rangle| = c_s(4\pi\rho/\beta)^{1/2}$, may be estimated from values of β that are constrained by the observations. The measured degree of velocity anisotropy is sen-
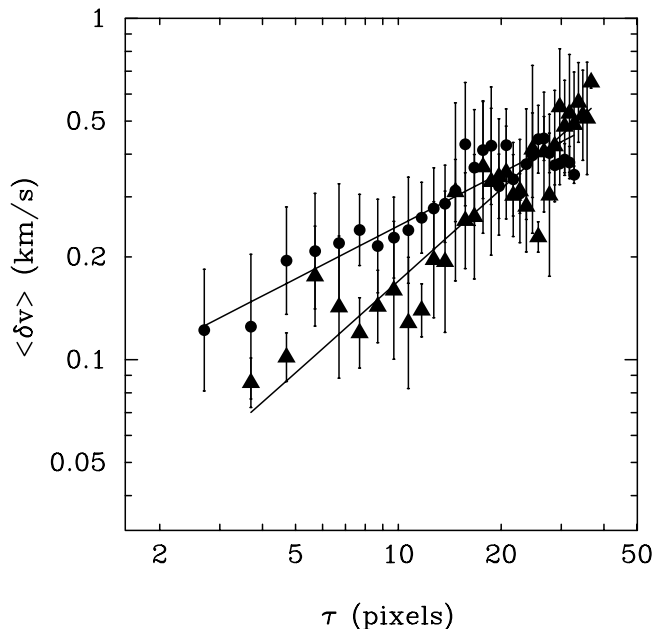

FIG. 5.—PCA-derived $\delta v, \tau$ relationship derived from the ^{12}CO spectroscopic data cube of the Taurus subfield rotated to align the x-axis with the angle of maximum anisotropy, $\theta_{\rm MAX} = 46°$. The triangles are points derived along the rotated x-axis, and the circles are points derived along the rotated y-axis. The error bars reflect the standard deviation of values in each bin. The pattern is similar to that found from the B2, B3 simulation snapshots in Fig. 2 and suggests an important role of the magnetic field in the local gas dynamics. [*See the electronic edition of the Journal for a color version of this figure.*]

sitive to the projected component of the mean field in the plane of the sky. It is improbable that the magnetic field threading an interstellar cloud is aligned in the sky plane. Therefore, measures of velocity anisotropy provide a lower limit to the value of B_0.

Based on our analyses, the anisotropy measured in the Taurus subfield is not as large as in the strong-field snapshots (B2, B3), but it is larger than the anisotropy limits for the intermediate-field strength model snapshots (C2, C3). Given this bracketing, we can assign an approximate value of $\beta = 0.03$ to the Taurus subfield as a logarithmic midpoint between the intermediate- and strong-field models. Since the observed region is within the low column density regime of the Taurus cloud, we set the kinetic temperature to be 15 K and the mean density to be 250 cm^{-3}. These values for the temperature and density are reasonably constrained by non-LTE excitation models that match the observed ^{12}CO and ^{13}CO $J = 1-0$ intensities from the subthermally excited component of the Taurus cloud (Goldsmith et al. 2008). The magnetic field strength corresponding to these values of β, kinetic temperature, and gas density is 14 μG. As noted above, this is a lower limit on the total magnetic field strength, since the velocity anisotropy is not sensitive to the line-of-sight component of the magnetic field.

Zeeman measurements of the OH line emission from the L1544 dark cloud, located $\sim 4°$ to the southwest of the subfield in Taurus, identify a line-of-sight field strength of 11 μG (Crutcher & Troland 2000). While this value is comparable to our coarse estimate of the field, these OH Zeeman observations are toward higher column density material [$N({\rm H}_2) \sim 2 \times 10^{22}$] than is likely present in the Taurus subfield. If this higher column density reflects a larger volume density and if the magnetic field is correspondingly compressed, the field in the diffuse parts of the Taurus cloud may be smaller.

The Chandrasekhar & Fermi (1953) method offers an additional measure of the magnetic field strength in interstellar clouds. It attributes deviations of the local magnetic field from the mean field direction to linear-amplitude transverse MHD waves such that

$$\delta B/B_p = |\delta v|/v_{\rm A}, \qquad (15)$$

where B_p is the projection of the mean magnetic field on the plane of the sky, δB and $|\delta v|$ are components of the magnetic and velocity perturbations transverse to B_p, and v_A is the Alfvén velocity. Assuming that polarization vectors accurately track the local magnetic field direction and that transverse velocity perturbations in the two directions perpendicular to $\hat{B}$ are comparable, the Chandrasekhar-Fermi method is rewritten in terms of observational measures,

$$\sigma_{\mathrm{pol}} = f(4\pi\rho_0)^{1/2}\sigma_v/B_p, \qquad (16)$$

where σ_{pol} is the dispersion of polarization angles measured in radians, σ_v is the line-of-sight velocity dispersion, ρ_0 is the mean density of the gas, and the factor f accounts for density inhomogeneity and line-of-sight integration. Ostriker et al. (2001) and Padoan et al. (2001) determine $f \approx 0.4-0.5$ from computational simulations. The dispersion of measured optical polarization angles within the target field is 0.17 rad. The line-of-sight velocity dispersion determined from the ^{13}CO data is 0.38 km s^{-1}. Assuming a mean density of 250 cm^{-3} and $f = 0.5$, the derived mean field strength is 14 μG. Thus, our PCA-based estimate of the magnetic field strength in Taurus also compares favorably to the value derived by the Chandrasekhar-Fermi method.

4.2. The Magnetic Support of the Taurus Cloud Envelope

The degree to which the magnetic field can support a volume against self-gravitational collapse is parameterized by the mass-to-flux ratio with respect to the critical value, $(M/\Phi)_{\mathrm{crit}} = 0.16/G^{1/2}$ (Nakano & Nakamura 1978). The magnetic critical index, μ, is the ratio of the mass-to-flux ratio of a volume to this critical value,

$$\mu = (M/\Phi)/(M/\Phi)_{\mathrm{crit}} = 7.6 \times 10^{-21} N(\mathrm{H}_2)/B, \qquad (17)$$

where $N(\mathrm{H}_2)$ is the gas column density in cm^{-2} along field lines and B is the magnetic field strength expressed in μG. Owing to projections of the magnetic field and the mass distribution along field lines, the observed index, μ_{obs}, overestimates the true magnetic index. Assuming random orientations of the magnetic field and flattened gas distribution with respect to the observer, one can derive a statistical correction to the observed value, $\langle\mu\rangle = \mu_{\mathrm{obs}}/3$, to assess whether a volume is supercritical ($\langle\mu\rangle > 1$) or subcritical ($\langle\mu\rangle < 1$; Heiles & Crutcher 2005).

Goldsmith et al. (2008) derive the distribution of molecular hydrogen over 100 deg^2 of the Taurus Molecular Cloud using the ^{12}CO and ^{13}CO $J = 1-0$ data of Narayanan et al. (2008). From the Goldsmith et al. (2008) image, the mean column density within the Taurus subfield analyzed in this study is 1.5×10^{21} cm^{-2}. For a magnetic field with strength 14 μG, this column density corresponds to an observed magnetic index of $\mu_{\mathrm{obs}} = 0.81$. Applying the statistical correction for projections, $\langle\mu\rangle = 0.27$. This low column density subfield within the Taurus cloud is magnetically subcritical, indicative of a magnetically supported cloud envelope. Such subcritical, low column density envelopes are expected given the exposure to the ambient UV radiation field that maintains a sufficient degree of ionization to couple the neutral material to ions. The ambipolar diffusion timescale is long with respect to the dynamical time of the envelope. While star formation within the high-density cores and filaments of the Taurus cloud attests to the gravitational collapse and lack of magnetic support within localized regions, these occupy a small fraction of the mass and area of the cloud. Goldsmith et al. (2008) report that 50% of the mass and 75% of the area of Taurus have molecular column densities less than 2×10^{21} cm^{-2}. If this column density regime is similar to the subfield analyzed in this study, then the Taurus molecular cloud envelope remains magnetically supported.

5. SUMMARY

We have developed an analysis method to assess velocity anisotropy within interstellar molecular clouds from spectroscopic imaging observations. Such anisotropy is predicted from theory of strong MHD turbulence (GS95). The utility of our method is demonstrated using MHD simulations with varying magnetic field strengths. Velocity anisotropy is recovered in models with strong magnetic fields ($\beta = 0.01$) oriented perpendicular to the line of sight. No anisotropy is measured in simulations with the magnetic field pressure more comparable to the local thermal pressure, or a few times larger ($\beta = 1.0, 0.1$). The analysis is applied to ^{12}CO $J = 1-0$ emission from a low-density subregion within the Taurus molecular cloud. We detect velocity anisotropy that is aligned within $\sim10°$ of the local magnetic field direction. This coincidence of the field direction with measured anisotropy in small-scale velocity variations demonstrates a strong coupling of the interstellar field with the neutral gas that may result from MHD turbulent flows. Our estimate of the plane-of-sky magnetic field strength based on our velocity anisotropy analysis is in agreement with the value derived using the Chandrasekhar-Fermi method. Based on our estimated magnetic field strength combined with column density measurements, we find that the low-density envelope of Taurus, which comprises the bulk of the cloud's mass, is magnetically subcritical.

REFERENCES

Brunt, C. M. 2003, ApJ, 584, 293
Brunt, C. M., & Heyer, M. H. 2002, ApJ, 566, 289
Brunt, C. M., Heyer, M. H., Vazquez-Semadeni, E., & Pichardo, B. 2003, ApJ, 595, 824
Brunt, C. M., & Mac Low, M. 2004, ApJ, 604, 196
Chandrasekhar, S., & Fermi, E. 1953, ApJ, 118, 113
Cho, J., Lazarian, A., & Vishniac, E. T. 2002, ApJ, 564, 291
Crutcher, R. M., & Troland, T. H. 2000, ApJ, 537, L139
Draine, B. T. 2003, ARA&A, 41, 241
Goldreich, P., & Sridhar, S. 1995, ApJ, 438, 763 (GS95)
Goldsmith, P. F., Heyer, M. H., Narayanan, G., Snell, R. L., Li, D., & Brunt, C. M. 2008, ApJ, 680, 428
Heiles, C. 2000, AJ, 119, 923
Heiles, C., & Crutcher, R. 2005, in Cosmic Magnetic Fields, ed. R. Wielebinski & R. Beck (Berlin: Springer), 137
Heyer, M. H., & Brunt, C. M. 2004, ApJ, 615, L45

Heyer, M. H., Ladd, E. L., & Carpenter, J. M. 1996, ApJ, 463, 630
Heyer, M. H., & Schloerb, F. P. 1997, ApJ, 475, 173
Maron, J., & Goldreich, P. 2001, ApJ, 554, 1175
Mouschovias, T. C. 1976, ApJ, 207, 141
Nakano, T., & Nakamura, T, 1978, PASJ, 30, 671
Narayanan, G., Heyer, M. H., Brunt, C. M., Goldsmith, P. F., Snell, R. L., & Li, D. 2008, ApJS, in press (arXiv: 0802.2556)
Ossenkopf, V., Esquivel, A., Lazarian, A., & Stutzki, J. 2006, A&A, 452, 223
Ostriker, E. C., Stone, J. M., & Gammie, C. F. 2001, ApJ, 546, 980
Padoan, P., Goodman, A., Draine, B. T., Juvela, M., Nordlund, A., & Rognvaldsson, O. E. 2001, ApJ, 559, 1005
Purcell, E. M. 1979, ApJ, 231, 404
Vazquez-Semadeni, E., Kim, J., & Ballesteros-Paredes, J. 2005, ApJ, 630, L49
Vestuto, J. G., Ostriker, E. C., & Stone, J. M. 2003, ApJ, 590, 858
Watson, W. D., Wiebe, D. S., McKinney, J. C., & Gammie, C. F. 2004, ApJ, 604, 707
Wiebe, D. S., & Watson, W. D. 2007, ApJ, 655, 275